ORIGINAL PAPER

Synergy of Viscosity Wedge and Squeeze Under Zero Entrainment Velocity in EHL Contacts

Bilel Meziane[1] · Nicolas Fillot[1] · Guillermo E. Morales-Espejel[1,2]

Abstract

In an elastohydrodynamic lubricated (EHL) contact under Zero Entrainment Velocity (ZEV) condition, surfaces cannot be separated by hydrodynamic lift. In this work, two other phenomena responsible for a film thickness build-up in ZEV contacts are studied using a numerical model. First, the thermal effect called "viscosity wedge" is investigated in steady-state conditions. Second, the "squeeze" effect is described in an environment where dynamic (time dependent) loads are considered. Then, both the viscosity wedge and squeeze effects are considered together. For each one of the two mechanisms, a characteristic time is considered. The ratio of these two times allows the identification of a dominant effect. Depending on this ratio, a prediction is attempted using semi-analytical models describing each effect. For an ideal set of parameters, it is shown that the combination of squeeze and viscosity wedge in EHL contact under ZEV allows for an enhanced performance.

Keywords Elastohydrodynamic · Zero entrainment velocity · Viscosity wedge · Squeeze

List of Symbols

Superscripts

A	Steady-state thermal conditions
B	Transient isothermal conditions
C	Transient thermal conditions
$*$	Semi-analytical formula

Subscripts

1,2	Solids 1 and 2, respectively
c	Central—film thickness
f	Fluid
m	Minimum—film thickness
min	Minimum—overtime

Variables (Unit)

a (m)	Dry contact radius(Hertz)
a_v (K^{-1})	Parameter for the Murnaghan density formula
a_{CY} (−)	Parameter for the Carreau–Yasuda non-Newtonian viscosity formula
A_1 (K)	Coefficient for the WLF viscosity correlation
A_2 (Pa^{-1})	Coefficient for the WLF viscosity correlation
B_1 (Pa^{-1})	Coefficient for the WLF viscosity correlation
B_2 (−)	Coefficient for the WLF viscosity correlation
C_1 (−)	Coefficient for the WLF viscosity correlation
C_2 (−)	Coefficient for the WLF viscosity correlation
C_p (J k g^{-1} K^{-1})	Heat capacity
E (Pa)	Young modulus
E' (Pa)	Material parameter
F (−)	Variable for the WLF viscosity correlation
G_{CY} (Pa)	Parameter for the Carreau–Yasuda non-Newtonian viscosity formula
h (m)	Film thickness
h_0 (m)	Rigid body separation
h_c^{Wang*} (m)	Transient semi-analytical formula for the prediction of h_c
h_m^{A*} (m)	Steady-state semi-analytical formula for the prediction of h_m
k (W m^{-1} K^{-1})	Thermal conductivity

✉ Nicolas Fillot
 nicolas.fillot@insa-lyon.fr

[1] Univ Lyon, INSA-Lyon, CNRS UMR5259, LaMCoS, 69621 Lyon, France

[2] SKF Research and Technology Development, 3992 AE Houten, The Netherlands

 ⚫ Springer

K_{00} (–)	Parameter for the Murnaghan density formula
K_M (–)	Parameter for the Murnaghan density formula
K'_M (–)	Parameter for the Murnaghan density formula
L (–)	Dimensionless Moes parameter
M (–)	Dimensionless Moes parameter
n_{CY} (–)	Parameter for the Carreau–Yasuda non-Newtonian viscosity formula
p (Pa)	Pressure
p_h (Pa)	Hertz contact pressure
Q (W m^{-3})	Total heat source
R (m)	Radius of curvature
R_{eq} (m)	Equivalent radius of curvature
t (s)	Time
t_{Final} (s)	Time at the end of calculation
$t_{Loading}$ (s)	Time at which the reference load is reached, the loading time
t_T (s)	Characteristic thermal time
$\bar{t}$ (–)	Dimensionless time
$\overline{t_{C\|m,\min}}$ (–)	Dimensionless instant at which the minimum value of the minimum film thickness is observed in transient thermal conditions
$\bar{t}_T$ (–)	Characteristic thermal–transient ratio
T (K)	Temperature
T_0 (K)	External temperature
T_g (K)	Glass transition temperature
T_{g0} (K)	Glass transition temperature at ambient pressure
T_R (K)	Reference temperature
u (m s^{-1})	Surface velocity
U_{DH} (–)	Dimensionless velocity parameter
w (N m^{-1})	Load per unit length
w_i (N m^{-1})	Initial load per unit length
w_{ref} (N m^{-1})	Reference load per unit length
x, y, z (m)	Coordinates
α^* (Pa^{-1})	Reciprocal asymptotic isoviscous pressure–viscosity coefficient
β_k (K^{-1})	Temperature–density parameter
δ (m)	Equivalent elastic surface displacement of both solids
η (m)	Dynamic viscosity
η_e (k g s^{-1} m^{-2})	Generalised viscosity parameter
η'_e (k g s^{-1} m^{-3})	Generalised viscosity parameter
λ^{Wang^*} (–)	Parameter for the transient central film thickness prediction formula
μ_g (Pa s)	Viscosity at glass transition
v (–)	Poisson coefficient
ρ (k g m^{-3})	Density
ρ_e (k g m^{-3})	Generalised density parameter
ρ'_e (k g s)	Generalised density parameter
$\rho_{e''}$ (k g m s)	Generalised density parameter
ρ_R (k g m^{-3})	Reference density
ρ^* (k g m^{-3})	Generalised density parameter
$\left(\frac{\rho}{\eta}\right)_e$ (m s)	Generalised density/viscosity ratio
τ_{zx} (Pa)	Shear stress along the x-axis
τ_e (Pa)	Shear stress norm

1 Introduction

In pure rolling conditions when the contacting surfaces move at the same velocity in the same direction, the behaviour of elastohydrodynamic lubricated (EHL) contacts is well understood. The semi-analytical formulae [1–9] written in such conditions indicate that the minimum film thickness in EHL contacts tend to decrease with the increase of the applied load. Similar conclusions have been made for contacts in rolling/sliding conditions [10, 11].

Under Zero Entrainment Velocity conditions (ZEV), that is when the contacting surfaces move at the same velocity and in opposite directions, no hydrodynamic lift can happen. Nonetheless, very high shearing implies that the thermal phenomenon called viscosity wedge needs to be considered. First introduced by Cameron in [12] regarding contacts in various sliding conditions, the viscosity wedge explains the pressure build-up in a ZEV contact by the close proximity of cold fluid at its two inlets (where both solids enter the contact) to heated fluid at its two outlets (where both solids exit the contact). This proximity leads to high vertical temperature gradients and by extension to viscosity gradients, themselves causing a pressure generation. ZEV contacts have received a lot of interest in the beginning of the millennia [13–17]. More recently, Zhang et al. [18, 19] have studied how surface roughness can influence the film thickness profile. Multiple authors have noted (in experiments and numerical simulations) that an increase of the load in EHL contact under ZEV condition leads to a small increase of the minimum film thickness [10, 20–23].

Another phenomenon, called squeeze effect, can contribute to the generation of pressure in lubricated contacts. It links a transient variation of film thickness with a time-dependent pressure generation. Pure squeeze, which happens when two solids with no tangential velocity are pressed together from an initial gap, presents three points of interest for the current work. First, the squeeze effect is time dependent and ultimately leads to no film thickness [24–27]). Second, when the initial gap is low enough, there is no rebound happening between the contacting bodies. Larsson and Hoglund [26] as well as Dowson and Wang [27] showed cases at high and low initial gaps exhibiting this behaviour. Third, whether there is rebound or not, while the minimum

film thickness decreases rapidly towards zero, the central film thickness hits a plateau [27–29].

Wall slip was evoked in the literature as potentially responsible for a load bearing capacity [30, 31]. Assuming industrial surfaces (not perfectly smooth), this effect is not supposed to happen and will therefore not be considered in this study.

The main objective of this work is to identify the main mechanisms that could explain a film thickness creation in ZEV contacts subjected to squeeze. Convincingly validated on a broad range of cases [23], EHL numerical models will be used to put into light the physics at stake and deliver local measurements. The viscosity wedge and squeeze effect will be characterised independently, before their combined effect is studied.

2 Model

2.1 Equations

The model used in this document is based on the ones provided by Raisin et al. [11] and Wheeler et al. [32]. The work by Habchi [33] gives more details on the numerical techniques employed. A 2D configuration is considered to describe cylinder on cylinder contacts with far less degrees of freedom than a full 3D configuration, while still providing accurate results (see [23] for a direct comparison between the configurations under stationary ZEV condition).

In this study, the two solids (1 and 2) in contact are assumed to be infinitely long cylinders aligned in the y-direction. As such, the problem is reduced to the plan (xz) where $\vec{x}$ is the axis of tangential movement of the solids and $\vec{z}$ the vertical axis where the film thickness is measured. Time is noted by the parameter t. Given the radii of curvature for the two solids R_1 and R_2, the equivalent radius of curvature R_{eq} is introduced as follows (see Eq. 1):

$$\frac{1}{R_{eq}} = \frac{1}{R_1} + \frac{1}{R_2} \tag{1}$$

A reference load w_{ref} is introduced. The Young modulus and Poisson coefficients of both solids are E_1, E_2, v_1 and v_2. The material parameter E' is defined as shown in Eq. 2:

$$\frac{2}{E'} = \frac{(1-v_1)^2}{E_1} + \frac{(1-v_2)^2}{E_2} \tag{2}$$

According to Hertz theory [34], when two infinitely long cylinders are pressed in dry conditions under the reference load w_{ref}, the zone of contact is an infinitely long band of width $2a$ (see Eq. 3):

$$a = \left(\frac{8w_{ref}R_{eq}}{\pi E'}\right)^{1/3} \tag{3}$$

Moreover, the solids are subjected to a parabolic pressure profile whose maximum value is the Hertz contact pressure p_h (see Eq. 4):

$$p_h = \frac{2w_{ref}}{\pi a} \tag{4}$$

Assuming a parabolic shape of the undeformed bodies, the film thickness h is given in Eq. 5:

$$h(x, t) = h_0(t) + \frac{x^2}{2R_{eq}} + \delta(x, t) \tag{5}$$

where h_0 is the rigid body separation, δ is the equivalent elastic surface displacement of both solids and $\frac{x^2}{2R_{eq}}$ the rigid solid geometry.

A Murnaghan [35] density law is considered (Eq. 6), describing the variation of density with pressure p and temperature T.

$$\rho(p, T) = \rho_R \frac{1}{\left(1 + \frac{K'_M}{K_M}p\right)^{-\frac{1}{K'_M}}} \frac{1}{1 + a_v(T_0 - T_R)} \tag{6}$$

where $K_M = K_{00}e^{-\beta_K T}$, with β_k the temperature–density parameter. All other parameters are controlled.

The Newtonian viscosity of the fluid, which represents its dependency with temperature and pressure only, is described by the improved WLF [36] correlation (Eq. 7):

$$\eta(p, T) = \eta_g \left(\frac{-2.303\, C_1(T - T_g)F}{C_2 + (T - T_g)F}\right) \tag{7}$$

where

$$T_g(p) = T_{g0} + A_1 \ln(1 + A_2 p)\ F(p) = (1 + B_1 p)^{B_2}$$

A_1, A_2, B_1, B_2 as well as C_1 and C_2 are the correlation parameters of the model. η_g is the viscosity at glass transition and T_{g0} the glass transition temperature at ambient pressure.

The non-Newtonian viscosity of the fluid, which described the behaviour of the fluid with the local shear stress, follows the model proposed by Carreau and Yasuda [37] (Eq. 8):

$$\eta(p, T, \tau_e) = \frac{\eta(p, T)}{\left(1 + \left(\frac{\tau_e}{G_{CY}}\right)^{a_{CY}}\right)^{\frac{\frac{1}{n_{CY}} - 1}{a_{CY}}}} \tag{8}$$

where

$$\tau_e = |\tau_{zx}|$$

τ_{zx} is the calculated shear stresses along the x-axis.

The film thickness is expected to be of a few hundred nanometres while the contact length on the other hand is expected to be of a few hundreds of micrometres. Therefore, the hypothesis of thin films is made. In addition, inertia forces and surface tension are considered negligible compared to viscous forces. Moreover, there will be no boundary slip at the solid/fluid interfaces. Finally, the flow is considered laminar. All of those assumptions lead to the Generalized Reynolds' equation [38] (Eq. 9):

$$\frac{\partial}{\partial x}\left(\left(\frac{\rho}{\eta}\right)_e \frac{\partial p}{\partial x}\right) - \frac{\partial \rho^*}{\partial x} - \frac{\partial \rho_e}{\partial t} = 0 \tag{9}$$

where $\rho_e = \int_0^h \rho dz$ $\rho'_e = \int_0^h \left(\rho \int_0^z \frac{dz'}{\eta}\right)dz$ $\rho''_e = \int_0^h \left(\rho \int_0^z \frac{z'dz'}{\eta}\right)dz$ $\frac{1}{\eta_e} = \int_0^h \frac{1}{\eta}dz$ and $\frac{1}{\eta'_e} = \int_0^h \frac{z}{\eta}dz$ a n d $\left(\frac{\rho}{\eta}\right)_e = \frac{\eta_e}{\eta'_e}\rho'_e - \rho''_e$, $\rho^* = \rho'_e \eta_e(u_2 - u_1) + \rho_e u_1$

In the following, the surface velocities are defined as follows: $u_2 = -u_1 = u$. This equation is solved in a one-dimensional domain $x \in [-6a; +6a]$. A condition of nil pressure is given at the two edges of the domain ($p = 0$). For more details on the stabilisation technique used and cavitation treatment employed, see the work by Habchi [33].

The calculated fluid pressure applies on top of an equivalent elastic solid, while the bottom edge is fixed (60a away from the lubricated contact, as in [33]). The elastic displacement of the top surface of the equivalent solid due to the fluid pressure is noted δ. Finally, $h_0(t)$ is calculated by solving the load balance equation.

$$\int_{-6a}^{6a} p\ dx = w(t) \tag{10}$$

Note that in this equation, no dynamic effects are considered.

The energy equation is written for both solids (subscripts 1 and 2) and for the fluid (subscript f), as in Eq. 11 and assuming that the heat source in the solids $Q_1 = Q_2 = 0$:

$$\frac{\partial}{\partial x}\left(k_i \nabla T\right) + \rho_i C_{pi}\left(u_i \frac{\partial}{\partial x}T + \frac{\partial T}{\partial t}\right) = Q_i \tag{11}$$

where k_i is the thermal conductivity, C_{pi} the thermal capacity and u_i the velocity of the subdomain (solids or fluid).

The transmission of energy through radiation is omitted as convection and conduction are considered prevalent. Moreover, the only heat sources are shear Q_s and compression Q_c heating occurring in the fluid, as given in Eq. 12:

$$Q_f = \underbrace{\eta\left(\frac{\partial u_f}{\partial x}\right)^2}_{s} + \underbrace{-\frac{T}{\rho}\frac{\partial \rho}{\partial T}\left(u_f \cdot \frac{\partial p}{\partial x}\right)}_{Q_c} \tag{12}$$

where u_f is the local velocity of the fluid.

Heat flux continuity is assumed at each fluid–solid interface, as in Eqs. 13 and 14:

$$k_f \left.\frac{\partial T}{\partial z}\right|_{z=0^+} = k_1 \left.\frac{\partial T}{\partial z}\right|_{z=0^-} \tag{13}$$

$$k_2 \left.\frac{\partial T}{\partial z}\right|_{z=h^+} = k_f \left.\frac{\partial T}{\partial z}\right|_{z=h^-} \tag{14}$$

The external temperature T_0 is imposed on the top and bottom boundaries of the solids. It is also ascribed to the side boundaries of the solids and fluid domains where the velocity vector points inwards. Everywhere else, a condition of nil flux is imposed.

The reader will refer to [11, 23, 33] for any details on the numerical procedure that are not recalled here. Figure 1 also illustrates the coupling between the dependent variables in the model and some of the important observed values such as the film thickness h and the viscosity η.

2.2 Operating Conditions

In this study, the lubricant is a commercial turbine (Shell T9) oil used in previous studies (see [23, 39, 40]). Table 1 gives all the parameters characterising this lubricant. The solids are made of steel (see Table 2). Operating conditions are given in Table 3.

The motion of the rolling elements of a full complement bearing is controlled by the overall dynamics of the bearing. Consequently, the inertia of the rolling elements is neglected at the scale of the contact. The loading process is modelled by controlling the load $w(t)$ [42, 43]. Only a single approach between the two bodies is considered. By doing so, only three loading parameters are needed to describe the loading process: the initial load w_i, the final load w_{ref} and the loading time $t_{Loading}$. The loading starts at $t = 0$. As such, the variation of load with time follows the description in Eq. 15:
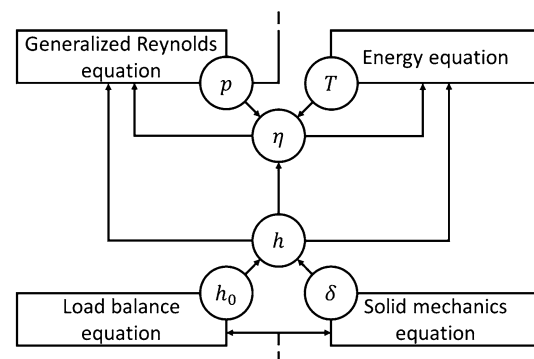

Fig. 1 Non-linear and highly coupled equations solved, as well as the corresponding dependent variables. The links between the various equations are shown

Table 1 Fluid properties from [39, 40]

Cp_f (J k g^{-1} K^{-1})]	1900
k_f (W m^{-1} K^{-1})	0.118
ρ_R (k g m^{-3})	872
K_{00} (Pa)	9.234×10^9
K_M'	10.545
a_v (K^{-1})	7.734×10^{-4}
β_k (K^{-1})	6.09×10^{-3}
η_g (Pas)	1×10^{12}
C1	15.9035
C2	14.1596
A1	188.95
A2 (Pa^{-1})	0.533×10^{-9}
B1 (Pa^{-1})	7.37×10^{-9}
B2	−0.6171
Tg_0 (K)	204.68
p_0 (Pa)	0
a_{CY}	5
n_{CY}	0.35
G_{CY} (Pa)	7×10^6
$T_R(K)$	298

Table 2 Solid properties are taken from [39, 41]

Parameter	Value
$E_1 = E_2 = E$ (Pa)	210×10^9
$\upsilon_1 = \upsilon_2 = \upsilon$	0.3
$\rho_1 = \rho_2 = \rho$ (k g m^{-3})	7850
$Cp_1 = Cp_2 = Cp$ (J kg^{-1} K^{-1})	470
$k_1 = k_2 = k$ (W m^{-1} K^{-1})	46

Table 3 Operating conditions

u (m s^{-1})	3
R_{eq} (m)	0.01
T_0 (K)	293.15
w_{ref} (N m)	100, 000

Table 4 Description of the model assumptions for each calculation case

	Case A: steady-state thermal	Case B: squeeze isothermal	Case C: squeeze thermal
Thermal effect	X		X
Squeeze effect		X	X

The model is used to simulate the contact while including or ignoring the thermal or squeeze effects. This will provide information on the independent effects of, respectively, the squeeze and viscosity wedge effects. Three cases are therefore considered, as reported in Table 4.

The viscosity wedge and squeeze effects are first studied separately, respectively, in Case A and Case B, in order to identify their respective influence on the behaviour of the contact under ZEV condition. Case C assumes that both effects are present.

When the squeeze effect is ignored, the results correspond to a series of steady-state cases (Case A). Each time $t < t_{\text{Loading}}$ corresponds to a load $w(t)$. It is possible to represent any dependent variable (such as the minimum film thickness $h_m(w(t))$) as a function of time, even though no transient effects are considered. For $t > t_{\text{Loading}}$, the steady-state case corresponds to the value obtained at $w = w_{\text{ref}}$.

The minimum film thickness in case A is noted $h_m^A(t)$ (and accordingly for superscripts B and C which refer to case B and case C, respectively). The notation $h_{m,\text{min}}^A$ refers to the minimum value of $h_m^A(t)$ over time. All previous definitions also apply to the central film thickness.

The dimensionless time $\bar{t}$ (Eq. 16) is introduced to study the influence of the loading time.

$$\bar{t} = \frac{t}{t_{\text{Loading}}} \tag{16}$$

Raisin et al. [11] defined a value of the thermal characteristic time for high slide-to-roll ratios in thermal transient problems as the ratio of the Hertz contact length a over the velocity of the fastest moving solid (In this case

$$\frac{w(t)}{w_{\text{ref}}} = \begin{cases} 0.67 \times 10^{-3} + \left(1 - 0.67 \times 10^{-3}\right)\frac{t}{t_{\text{Loading}}} & \text{for } t < t_{\text{Loading}} \\ 1 & \text{for } t_{\text{Loading}} \leq t < t_{\text{Final}} \end{cases} \tag{15}$$

where $t_{\text{Final}} = 100 \times t_{\text{Loading}}$ is chosen so that the stead state is reached in all studied cases.

The value of $w_i = 0.67 \times 10^{-3} \times w_{ref}$ was chosen to ensure that the initial state was in the hydrodynamic regime (with deformations negligible compared to the film thickness), with extremely low temperature gradients while still being a converged result using the current model.

$|u_1| = |u_2| = u$). However, their definition of a was based on an average value of the contact load. As such, the definition of the thermal characteristic time must be adapted to the present study. The final load is therefore chosen as a reference for its definition. This leads to the definition of the thermal characteristic time given in Eq. 17.

$$t_T = \frac{a}{u} = 0.07 \text{ ms} \tag{17}$$

The ratio $\bar{t}_T = t_T/t_{\text{Loading}}$ represents the relative influence of the thermal effects compared to the squeeze effect. It is called the characteristic thermal–transient ratio.

2.3 Initial State

In cases A and C where thermal effects are considered, the initial state is defined by a steady-state thermal result (with $w = w_i = 0.67 \times 10^{-3} \times w_{\text{ref}}$). This initial state presents two particularities. First, the maximum elastic surface displacement (2 nm) is negligible compared to the film thickness (0.3%), which corresponds to a thermal hydrodynamic regime. Second, the temperature in the entire fluid

is subjected to very small variations, which are enough to ensure a stable film thickness under this very small load.

The corresponding temperature distribution is represented in Fig. 2a. The maximum temperature is extremely small compared to temperature differences found in highly loaded contacts under ZEV condition (see Fig. 2b). The minimum film thickness (in Case A and C) is $h_m^A(t = 0) = h_m^C(t = 0) = 529$ nm. The film thickness is not null because of temperature gradients, albeit small, between the two contacting surfaces. The maximum contact pressure is only 0.372 MPa.

As depicted in Fig. 2, the shape of film thickness profile will drastically change from the small initial load (Fig. 2a, hydrodynamic regime) to the final load (Fig. 2b, Elastohydrodynamic regime), where a dimple (local maximum of film thickness) forms at the centre of the contact, and two
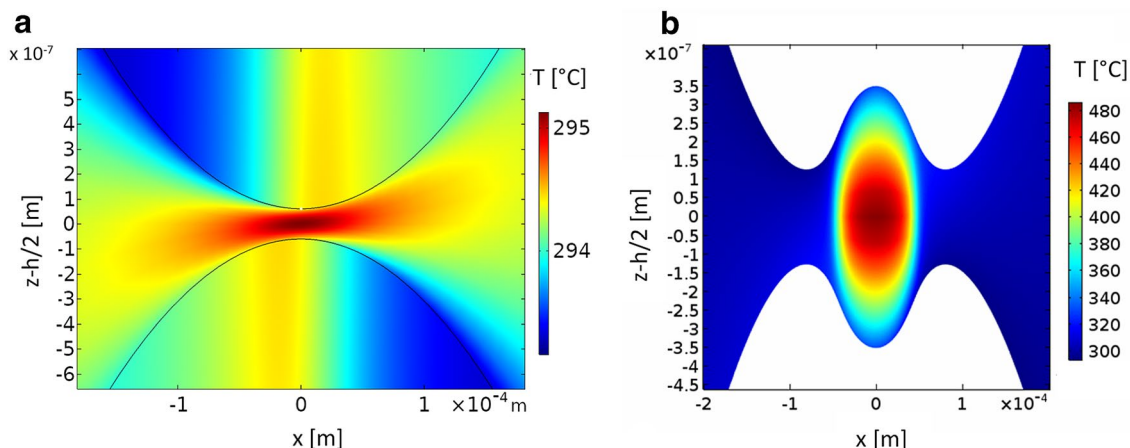

Fig. 2 Film thickness and temperature profiles in the **a** initial and **b** final states, with respective load ales on axes and colour map $w_i = 0.67 \times 10^{-3} \times w_{\text{ref}}$ and $w_{\text{ref}} = 100,000$ N m^{-1}. Scales on axes and colour map are not the same to emphasize the temperature gradient in the film thickness. For the same reason, temperature map is not plotted on the solids in (**b**)

Fig. 3 Variation of the central and minimum film thicknesses with the load in case A. The semi-analytical model described in Eqs. 19 and 20 is shown in red. A better view of the different observed values is provided for lower loads between 0 and 2500 N m^{-1}. Horizontal lines, in grey, show the minimum value $h_{m,\text{min}}^A$ and the final value $h_m^A(w_{\text{ref}})$

Minimum film thickness (numerical)
Central film thickness (numerical)
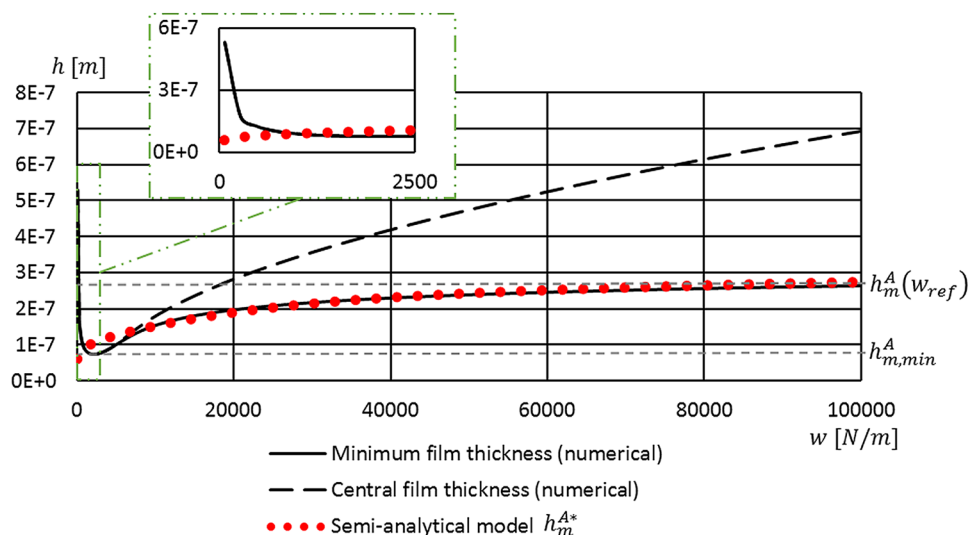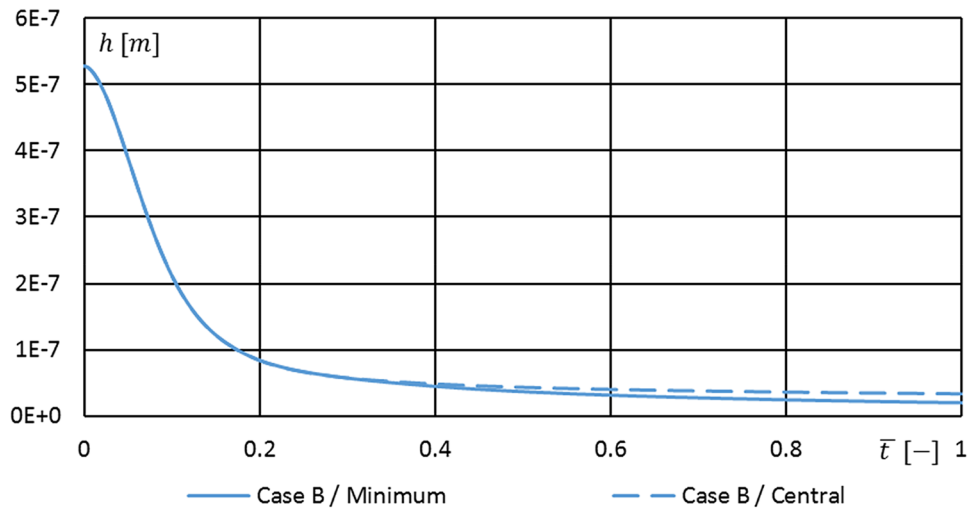Semi-analytical model h_m^{A*}

Fig. 4 Variation of the minimum and central film thicknesses in case B, for $t_{\text{Loading}} = 1\text{ms}$. The decrease of both the central and minimum film thicknesses can be seen in the entire domain

minima appear the inlet/outlet of the contact, as previously described in [17–23].

The thermal aspect of the model is not considered in case B. As such, the initial state is defined by fixing h_0 to the same value (527 nm) as in cases A and C. The consequence is that there is no pressure and no elastic displacement in the initial state for case B. Given the small initial gap, no rebound is expected [26, 27].

3 Individual Effects of Viscosity Wedge and Squeeze

3.1 Case A: Thermal Steady-State Viscosity Wedge

The variation of the film thickness in case A with the load is represented in Fig. 3.

As the load increases from $w = 67$ to $w = 2065.7\,\text{N}\,\text{m}^{-1}$, the value of the minimum and central film thicknesses decreases down to $h_{m,\text{min}}^A = 74\text{nm}$. This is associated with a rigid body separation h_0 decrease of 401 nm, far stronger than the increase (61.4 nm) of the elastic surface displacement δ (see Eq. 5). This behaviour corresponds to a thermal hydrodynamic lubrication (THL) regime. No dimple is observed during this phase.

From $w^{1D} = 2065.7\,\text{Nm}^{-1}$ onward, an increase of the load is associated with an increase of the minimum film thickness. This corresponds to an elastic surface displacement δ varying in the same order of magnitude as the rigid body separation h_0. This indicates an EHL regime. From a physical point of view, an increase of the load leads to an increase of the pressure in the contact. This, in turn, is the cause for a stronger shear heat generation. Higher vertical thermal gradients of temperature ensue, which ultimately

induce higher vertical viscosity gradients. As indicated by the Navier–Stokes equation [44] written in 1D assuming thin films (see Eq. 18), this leads to higher pressure gradients, and as such, a stronger viscosity wedge. For an in depth analysis of this behaviour, see [23].

$$\frac{\partial p}{\partial x} = \frac{1}{h}\int_0^h \frac{\partial p}{\partial x}dz = \frac{1}{h}\int_0^h \frac{\partial(\eta\dot\gamma)}{\partial z}\mathrm{d}z = \frac{(\eta\dot\gamma)_h - (\eta\dot\gamma)_0}{h} = \frac{\Delta(\eta\dot\gamma)}{h}$$
(18)

At $w = 5263.5\,\text{Nm}^{-1}$, the central and minimum film thickness are dissociated. From there, a dimpled film thickness profile is observed for all loads. Figure 3 shows how the increase of the central film thickness with the load is stronger than the increase of the minimum film thickness. These results qualitatively corroborate the ones obtained in other studies [10, 22].

The red dotted line in Fig. 3 shows the prediction h_m^{A*} of the semi-analytical model developed in Eqs. 19 and 20, inspired from [23] and adapted to steel–steel contacts. The method of least squares was used, with a coefficient of determination of 0.96 for the experimental dataset and 0.98 for the numerical one. For more details on this equation, refer to Appendix. This model captures well the case of this study but it is not universal since it does not include the material properties, nor the external temperature (here $T_0 = 293.15\,\text{K}$), these parameters playing a major role as shown in [23].

$$\frac{h_m^{A*}(u, w, R_{\text{eq}})}{h^*} = w^{0.146} \times \left(\frac{R_{\text{eq}}}{R^*}\right)^{-0.42} \times (1 - \exp(-u/u^*))$$
(19)

$$\frac{u^*}{u_0} = 1 + \exp\left(-\frac{w}{w_0}\right)$$
(20)

Fig. 5 Variation of the minimum film thicknesses with $\bar{t}$ in case B for all values of t_{Loading}
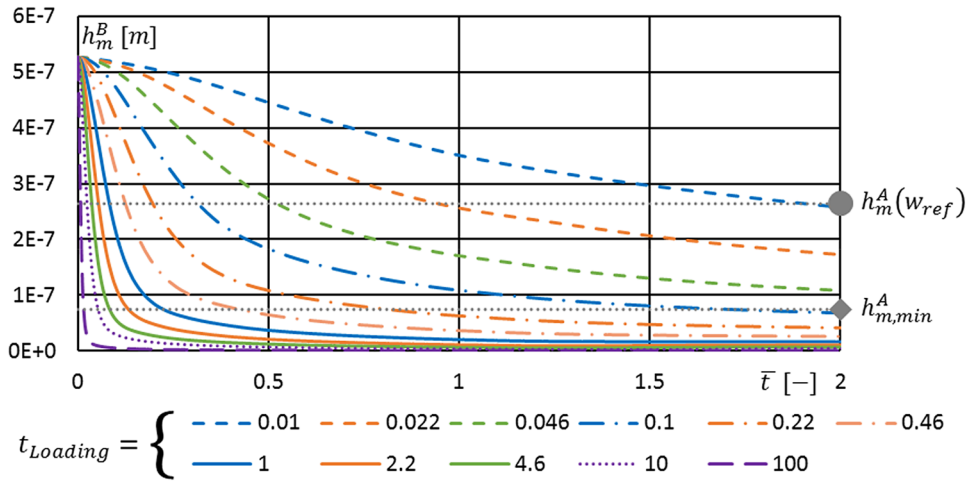
Table 5 Parameters used to predict the central film thickness in case B, using the semi-analytical formula by Wang et al. [28]

a (m)	p_h (Pa)	η_0 (Pas)	α^* (Pa^{-1})
1.05×10^{-4}	6.06×10^8	0.0195	2.36×10^{-8}

where w is expressed in Nm^{-1}, $h^* = 69.8$ nm, $R^* = 0.0128$ m, $u_0 = 2.74$ m s^{-1}, $w_0 = 14695$ N m^{-1}. This semi-analytical model fits the numerical results obtained in Fig. 3 with a good accuracy (for $w^{1D} > 8000$ N m^{-1}, the maximum relative difference between h_m^{A*} and h_m is 6.12%).

By itself, the viscosity wedge in ZEV condition is able to provide a stable long-term film thickness. However, the transition from the HL regime to the EHL regime is marked by a low value of the minimum film thickness $h_{m,\min}^A$.

3.2 Case B: Isothermal Squeeze

Figure 4 shows the variation of the central and minimum film thicknesses in case B for $t_{\text{Loading}} = 1 ms$. Both values continuously decrease over time. A strong initial decrease of the film thickness during the early stages of the loading process is observed. When the dimple is formed, the central film thickness barely decreases anymore, while the minimum film thickness is continuously decreasing towards zero. These results are reminiscent of those obtained by Dowson and Wang [27] in the case of a very small drop height.

The variation of the minimum film thickness is represented in Fig. 5 (as a function of $\bar{t}$) for different loading times. In all cases, the film thickness decreases with the loading time. The decrease of the minimum film thickness is quicker—relatively to the loading time—for higher loading times. In this Figure, the maximum load is always reached at $\bar{t} = 1$. For $t_{\text{Loading}} = 0.01 ms$, the minimum film thickness has decreased by 33.4% when the maximum load is reached.

Table 6 Values of the central film thickness adapted from Wang et al. [28] compared to the central and minimum values given by the current model in case B, for various loading times, at $\bar{t} = 1$ Thicknesses in nm

t_{Loading}(ms)	$h_c^{\text{Wang}^*}$	h_c^B	$\left\vert\frac{h_c^B - h_c^{\text{Wang}^*}}{h_c^{\text{Wang}^*}}\right\vert$ (%)	h_m^B	$\left\vert\frac{h_m^B - h_c^{\text{Wang}^*}}{h_c^{\text{Wang}^*}}\right\vert$ (%)
0.01	404.6	351.0	13.3	351.0	13.3
0.022	264.8	256.4	3.2	256.4	3.2
0.046	178.2	172.4	3.2	170.7	4.2
0.1	117.4	117.5	0.1	108.8	7.3
0.22	76.8	76.3	0.6	62.9	18.1
0.46	51.7	51.1	1.2	36.4	29.6
1	34.0	34.1	0.2	20.3	40.5
2.2	22.3	23.0	3.3	10.8	51.7
4.6	15.0	15.6	3.9	6.3	58.2
10	9.9	10.5	6.4	3.4	66.0
100	2.9	3.2	13.0	0.7	74.4

In contrast, for $t_{\text{Loading}} = 100 ms$, the minimum film thickness has decreased by 99.8%.

Wang et al. [28] developed a semi-analytical model to account for an impact with initial velocity and no gravity. The dimensionless Moes parameters are defined in Eq. 21, and the film thickness formula defined by Wang et al. [28] is adapted in Eq. 22 (superscript Wang*) by replacing the maximum half width, load and hertz pressure by their values at the end of the load ramp. The reciprocal asymptotic isoviscous pressure–viscosity coefficient α^* is used to adapt to the usage of the WLF viscosity correlation as defined by Bair [45]. All complementary values are reported in Table 5.

$$\begin{cases} M = \pi \left(\frac{3}{4\lambda^{\text{Wang}^*}}\right)^{\frac{1}{2}} \\ L = \alpha^* p_h \left(\frac{4\lambda^{\text{Wang}^*}}{3}\right)^{\frac{1}{4}} \end{cases} \tag{21}$$

where $\lambda^{\text{Wang}^*} = \frac{12 \times \eta_0 \times R_{eq}^2}{a \times p_h \times t^*}$ and $t^* = t_{\text{Loading}}$

$$\frac{h_c^{\text{Wang}^*}}{R_{eq} \times \left(U_{\text{DH}}\right)^{1/2}} = 2.3 \times M^{0.2} \times L^{0.55}$$

(22)

where $U_{DH} = \frac{1}{2}\left(\frac{L}{\alpha^* E'}\right)^4$

Table 6 contains the values of $h_c^{\text{Wang}^*}$, $h_c^B\left(\bar{t}=1\right)$ and $h_m^B\left(\bar{t}=1\right)$ for all values of t_{Loading}. They are also plotted in Fig. 6 for comparison. For loading times such as $0.046\text{ ms} < t_{\text{Loading}} < 4.6\text{ ms}$, the relative difference is less than 4% for the central film thickness. The formula adapted from Wang et al. [28] is in good agreement with the results of the present model for the central film thickness.

For $0.01\text{ ms} < t_{\text{Loading}} < 0.22\text{ms}$, the relative difference is less than 18.1%. Beyond that, the film thickness is itself below 50nm. As such, even though the relative difference between values increases, the absolute difference stays below 16nm.

For slow loading processes, the film thickness at maximum load is of a few nanometres, whereas fast loading processes lead to values of a few hundred nanometres. Therefore, the present results highlight the fact that stronger loading processes lead to a relatively stronger squeeze effect.

4 Case C: Synergy Between the Viscosity Wedge and Squeeze Effects

In this section, assuming both squeeze and viscosity wedge are present (Case C), the behaviour of the contact is studied and compared to Case A and Case B. The initial and temporary squeeze effect is compared to the onset of viscosity wedge effect.

Fig. 6 Variation of the minimum (full line) and central (dashed line) film thicknesses at $\bar{t}=1$ as a function of the loading time t_{Loading}, compared to the semi-analytical model (black crosses) adapted from Wang et al. [19] (see Eqs. 21 and 22). The numerical values are listed in Table 6
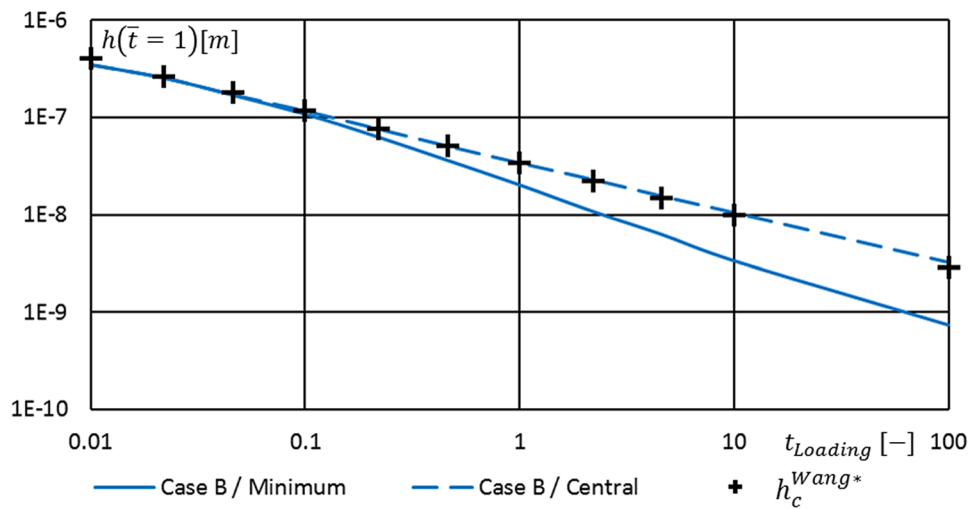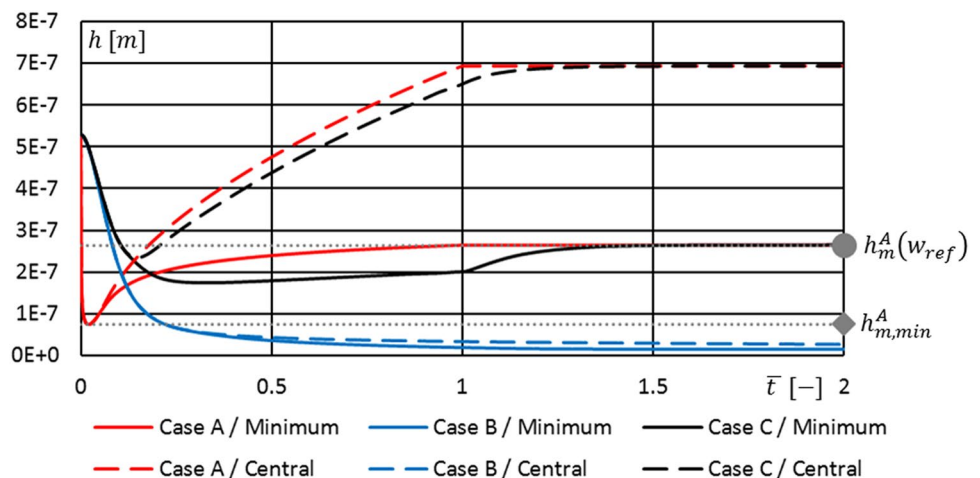

Fig. 7 Variation of the central and minimum film thicknesses in cases A, B and C, as a function of the dimensionless time $\bar{t}$. The maximum load is reached at $\bar{t}=1$

Fig. 8 Variation of the minimum film thickness in case A and case C, for $\bar{t}_T = \{0.0007, 0.007, 0.0152, 0.0318, 0.07\}$, as a function of the dimensionless time $\bar{t}$. The minimum values over time are marked with "x". $h^A_{m,\text{min}}$ and $h^A_m(w_{\text{ref}})$, respectively, represent the minimum film thickness over time and the film thickness at maximum load in case A
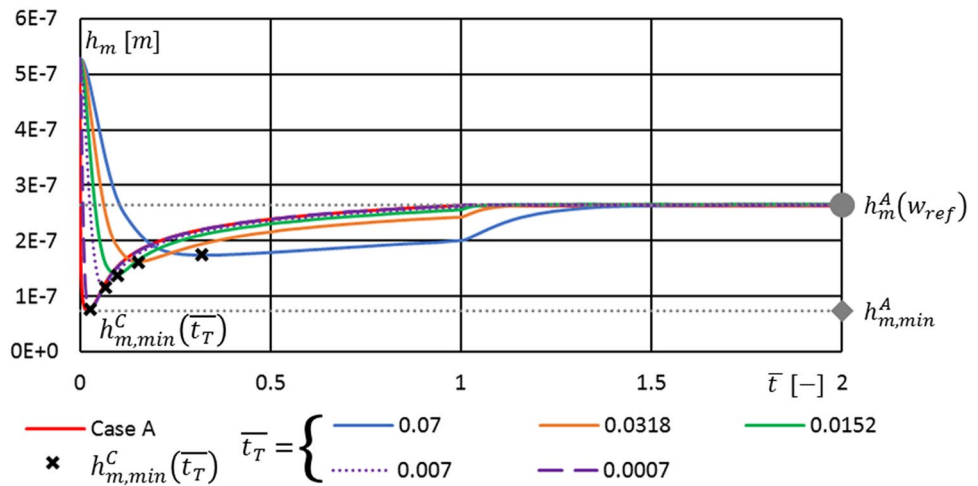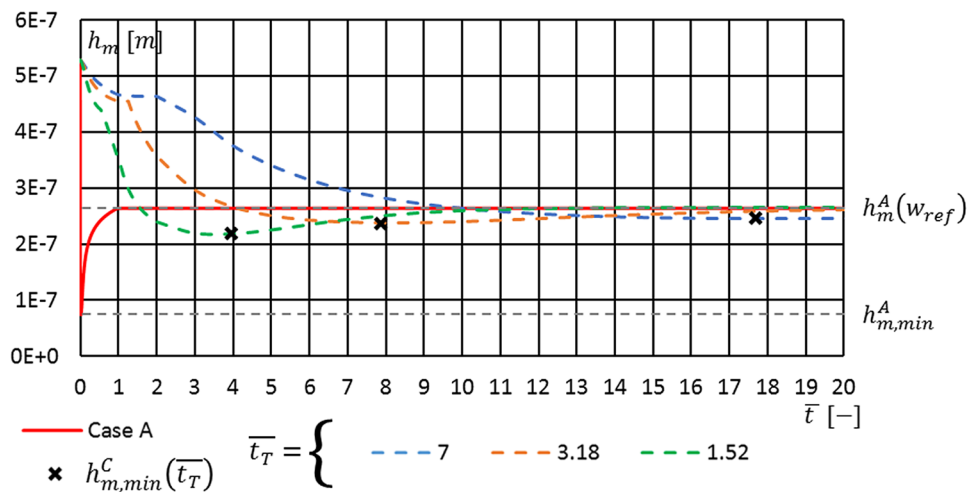

Fig. 9 Variation of the minimum film thickness in case A and case C, for $\bar{t}_T = \{1.52, 3.18, 7\}$, as a function of the dimensionless time $\bar{t}$. The minimum values are marked with "x"

4.1 Reference Case

The variations of the central and minimum film thicknesses for $t_{\text{Loading}} = 1\,\text{ms}$ in cases A, B and C are represented in Fig. 7.

When the squeeze and thermal effects are considered in case C, both the minimum and central film thicknesses follow a non-monotonous variation with time. At the beginning of the loading process, the central and minimum film thicknesses are the same, until $\bar{t} = 0.124$. Before that, while case A rapidly reaches a minimum value at $\bar{t} = 0.02$, the decrease in case C closely follows the shape of case B, with a relative difference between the minimum film thicknesses in cases B and C of 0.6%. The squeeze effect is the main reason for the high film thickness at the early stages of case C.

Around $\bar{t} = \bar{t}_T = 0.07$, the merged minimum and central film thicknesses in case C decrease at a slower rate than in case B. At this stage, meaningful thermal effects appear. Moreover, the load is high enough ($w = 7062.3\,\text{N m}^{-1}$) so that the corresponding merged minimum and central film

thicknesses in case A are in the EHL regime, which is associated with an increase of the film thickness with the load.

At $\bar{t} = 0.124$, separation between the central and minimum film thicknesses occur, marking the appearance of a central dimple.

While the minimum film thickness is continuously decreasing in case B, the minimum film thickness in case C ($h^C_{m,\text{min}} = 175\,\text{nm}$) is reached at $\bar{t} = 0.372$, this time being 18.6 times greater than the one to reach $h^A_{m,\text{min}}$, for a film thickness 2.35 times greater.

As can be seen in Fig. 7, the sudden stop in the loading process (at $\bar{t} = 1$) induces a sudden change of the variation of h^C_m. Indeed, at the instant the final load is attained, the transient term in Reynolds equation (Eq. 9) becomes close to zero, although not nil since the film thickness is still varying at that instant. The steady state is reached at $\bar{t} = 1.368$.

This reference case shows how the squeeze and the viscosity wedge effects are complementary to ensure a separation of the solids involved in a load ramp under ZEV condition. The squeeze effect provides an initial but temporary

load bearing capacity, delaying the otherwise rapid drop to very small film thicknesses at small loads. This dampening is similar to the one observed by Vichard [46]. Moderate-to-high loads lead to the emergence of a stronger viscosity wedge effect.

4.2 Influence of the Characteristic Thermal–Transient Ratio

The effect of the loading time (for a given thermal characteristic time) is analysed in this section. The variation of the minimum film thickness with the dimensionless time $\bar{t}$ is represented in Figs. 8, 9 and 10 for various thermal–transient ratios. The values of $h_{m,\min}^{C}$ are reported in Fig. 11 for all values of $\bar{t}_T = t_T / t_{\text{Loading}}$.

4.2.1 Slow Loading

For extremely slow loadings ($t_{\text{Loading}} = \{10, 100\}ms$ which corresponds to $\bar{t}_T \leq 0.007$), the thermal time is extremely small compared to the loading time, which means that the thermal equilibrium stays close to the steady-state contact (case A). In these cases, the minimum film thickness over time $h_{m,\min}^{C}$ tends towards the value $h_{m,\min}^{A} = 74nm$ for the biggest loading times.

For slow loadings ($t_{\text{Loading}} = \{1, 2.2, 4.6\}ms$ which corresponds, respectively, to $\bar{t}_T = \{0.0152, 0.0318, 0.07\}$), the squeeze effect provides a higher film thickness for a longer relative time during the loading process. This means that during the initial state (small load corresponding to the THL regime), the minimum film thickness is well over the value of the steady-state case ($h_m^C > h_m^A$). From then, the behaviour of the contact is similar to the steady-state case, as described in the previous section. As the characteristic

Fig. 10 Variation of the minimum film thickness in cases A, B and C, for $\bar{t}_T = \{0.152, 0.318, 0.7\}$, as a function of the dimensionless time $\bar{t}$. The minimum values over time $h_{m,\min}^{C}$ are marked with a "x" in the corresponding colour. The prediction formula adapted from Wang (see Eqs. 21 and 22) is also marked with a "+" as a reference. $h_{m,\min}^{A}$ and $h_m^A(w_{\text{ref}})$ respectively represent the minimum value over time and the value at maximum load in the steady-state case
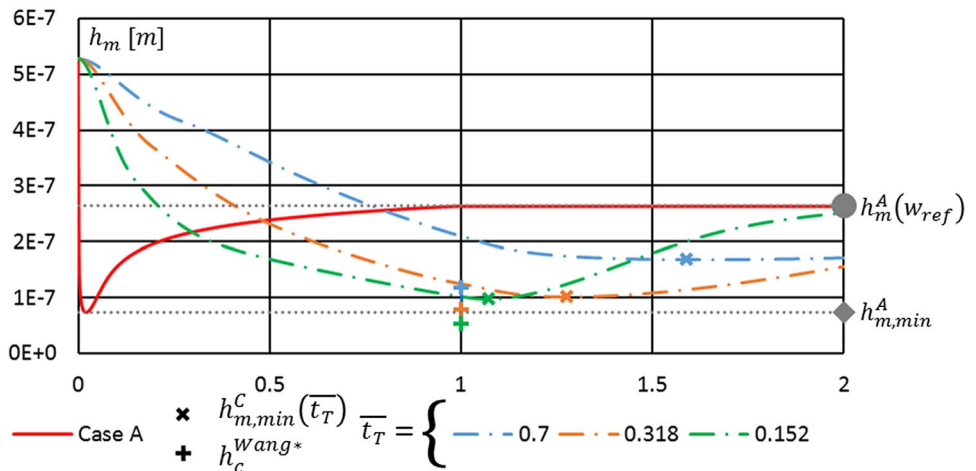

Fig. 11 Minimum film thickness over time in case C, as a function of the characteristic thermal–transient ratio. The horizontal dotted lines mark the two extrema of the steady-state case A. The semi-analytical formula for case A (see Eqs. 19 and 20) and the prediction formula adapted from Wang (see Eqs. 21 and 22) are given as references in red and blue, respectively. The black line corresponds to a composite model (Eq. 27) accounting for three regimes named "Slow", "Intermediate" and "Fast" loading
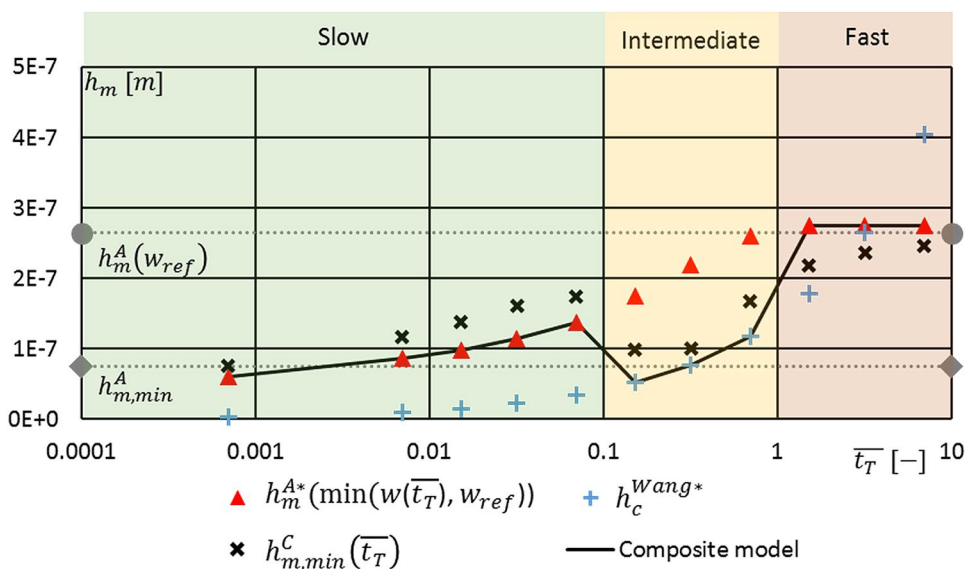
Table 7 Tentative prediction of the minimum film thickness (in [nm]) over time for slow loadings. Each relative difference is calculated assuming $h^C_{m,min}$ as a reference

$\bar{t}_T$	0.0007	0.007	0.0152	0.0318	0.07
$h^C_{m,\min}$	76	116	138	161	174
$(\overline{t_{C|m,\min}})$	0.03	0.07	0.10	0.15	0.32
$h^A_m(\overline{t_{C|m,\min}})$	76	123	154	183	221
$\frac{h^C_{m,\min}-h^A_m(\overline{t_{C|m,\min}})}{h^C_{m,\min}}$	< 1%	6%	12%	13%	27%
$h^{A*}_m(w(\overline{t_{C|m,\min}}))$	110	136	152	174	219
$\left\|\frac{h^C_{m,\min}-h^{A*}_m(w(\overline{t_{C|m,\min}}))}{h^C_{m,\min}}\right\|$	43%	17%	10%	8%	26%
$h^{A*}_m(w(\bar{t}_T))$	61	86	98	114	138
$\left\|\frac{h^C_{m,\min}-h^{A*}_m(w(\bar{t}_T))}{h^C_{m,\min}}\right\|$	21%	26%	29%	29%	21%

All film thicknesses are given in nm

thermal–transient ratio $\bar{t}_T$ increases, the relative time needed to reach the steady-state state (after the loading ramp) increases.

In Fig. 8, the minimum film thickness in case C, noted $h^C_{m,\min}$, is particularly close to the curve describing the minimum film thickness in case A. For each $h^C_{m,\min}$ value corresponds a specific time noted $\overline{t_{C|m,\min}}$, as shown in Table 7. For each of these times corresponds an instantaneous load $w(\overline{t_{C|m,\min}})$, and by extension a value of the film thickness in steady-state conditions. Different approximations are attempted in Table 7.

First, the comparison between $h^C_{m,min}$ and $h^A_m(\overline{t_{C|m,\min}})$ shows that the values given by the model in case A overestimate the values given in case C by less than 13% for $\bar{t}_T \leq 0.0318$ and 27% for $\bar{t}_T = 0.07$. A first approximation in this range of values, therefore that $h^A_m(\overline{t_{C|m,\min}})$, is close to $h^C_{m,min}$.

A more tentative comparison is to use $w(\overline{t_{C|m,\min}})$ as an input in the semi-analytical model given in Eqs. 19 and 20, which gives the values $h^{A*}_m(w(\overline{t_{C|m,\min}}))$. The relative differences between $h^C_{m,\min}$ and $h^{A*}_m(w(\overline{t_{C|m,\min}}))$ are below 26% for $\bar{t}_T \geq 0.007$. For $\bar{t}_T = 0.0007$, the relative difference is quite higher at 43%, which can be explained by the shortcomings of the semi-analytical model in extremely low load conditions. Indeed, the value of $h^C_{m,\min}$ at $\bar{t}_T = 0.0007$ corresponds to a transition between the hydrodynamic and elastohydrodynamic regimes. This transition is not predicted by the semi-analytical model previously proposed. The resulting error is therefore unavoidable, but still acceptable at first approximation. A second approximation for slow loadings is therefore that $h^{A*}_m(w(\overline{t_{C|m,\min}}))$ is close to $h^C_{m,\min}$.

The previous analysis rely on the measured value $\overline{t_{C|m,\min}}$. As an attempt to provide an approximation that is independent on any simulation results, the value of $\bar{t}_T$ is chosen. As such, $w(\bar{t}_T)$ is used as an input in the semi-analytical model given in Eqs. 19 and 20, giving a minimum film thickness prediction $h^{A*}_m(w(\bar{t}_T))$. While the values of $\bar{t}_T$ differ from $\overline{t_{C|m,\min}}$ by close to an order of magnitude, the resulting comparisons between $h^C_{m,\min}$ and $h^{A*}_m(w(\bar{t}_T))$ show relative differences less than 29%.

$$h^C_{m,\min} \approx h^{A*}_m(w(\bar{t}_T)) \tag{23}$$

4.2.2 Fast Loading

For fast loadings on the other hand ($t_{\text{Loading}} = \{0.01, 0.022, 0.046\}ms$ which corresponds to $\bar{t}_T > 1.52$), the transient effect is so strong that the minimum film thickness in case C is greater than in case A at least until the maximum load is reached (Fig. 9), and then it continues to decrease towards $h^A_m(w_{\text{ref}})$.

A general approximation can be made for this type of loadings, by assuming that the minimum film thickness over time $h^C_{m,\min}$ is close to the value of the steady state at full load, which can be approximated by the semi-analytical model (see Eqs. 19 and 20):

$$h^C_{m,\min} \approx h^{A*}_m(w_{\text{ref}}) \tag{24}$$

With this assumption, the relative differences between the simulations and the semi-analytical model are between 12 and 26%, as shown in Table 8.

4.2.3 Intermediate Loading

For intermediate loadings ($t_{\text{Loading}} = \{0.1, 0.22, 0.46\}ms$ which corresponds to $\bar{t}_T \in \{0.152, 0.318, 0.7\}$), the squeeze effect is still visible in Fig. 10. For this type of loading, the

Table 8 Tentative prediction of the minimum film thickness over time for slow loadings

$\bar{t}_T$	1.52	3.18	7
$h^C_{m,\min}$	218	237	245
$h^{A*}_m(w_{\text{ref}})$	275	275	275
$\left\|\frac{h^C_{m,\min}-h^{A*}_m(w_{\text{ref}})}{h^C_{m,\min}}\right\|$	26%	16%	12%

Table 9 Tentative prediction of the minimum film thickness over time for slow loadings

$\bar{t}_T$	0.152	0.318	0.7
$h^C_{m,\min}$	98	100	167
$h^{\text{Wang}*}_c$	51	78	117
$\left\|\frac{h^C_{m,\min}-h^{\text{Wang}*}_c}{h^C_{m,\min}}\right\|$	48%	23%	30%

minimum film thickness is observed above $\bar{t} = 1$. It is therefore possible to assume that the minimum film thickness over time $h^C_{m,\min}$ is at least above the value obtained when only the squeeze effect is considered $h^B_m(\bar{t} = 1)$.

The thermal viscosity wedge, though influencing the result, is not yet fully active because of the fast load ramp compared to the thermal characteristic time ($\bar{t}_T < 0.7$). The minimum film thickness in case C is then smaller than $h^A_m(w_{\mathrm{ref}})$ before the end of the ramp.

As a consequence, and considering the previous approximation on Case A and Case B with semi-analytical formulae, $h^C_{m,\min}$ would verify Eq. 25:

$$h^{\mathrm{Wang}^*}_c < h^C_{m,\min} < h^{A*}_m(w_{ref}) \tag{25}$$

As described in Table 9, $h^C_{m,\min}$ is closer to the lower limit, so as an approximation

$$h^C_{m,\min} \approx h^{\mathrm{Wang}^*}_c \tag{26}$$

Under this assumption the relative difference is between 22.6 and 47.6%, still capturing the good order of magnitude.

4.2.4 A Composite Model Depending on the Thermal–Transient Ratio

Figure 11 shows the minimum film thickness over time $h^C_{m,\min}$, for each value of the characteristic thermal–transient ratio $\bar{t}_T$. The three regions previously studied are easily identified. The slow region, for which a good approximation is $h^{A*}_m(w(\bar{t}_T))$, the intermediate region, better fitted with $h^{\mathrm{Wang}^*}_c$, and the fast region where the asymptote corresponds to $h^{A*}_m(w_{\mathrm{ref}})$.

The different asymptotes and analytical predictions are plotted with different colours, and a composite model is proposed (black line in Fig. 11), according to the thermal–transient ratio $\bar{t}_T$, covering all cases in Eq. 27.

$$h^C_{m,\min} \approx \begin{cases} h^{A*}_m\left(w(\bar{t}_T)\right) & \text{for } \bar{t}_T \leq 0.1 \\ h^{\mathrm{Wang}^*}_c & \text{for } 0.1 < \bar{t}_T < 1 \\ h^{A*}_m\left(w_{ref}\right) & \text{for } \bar{t}_T \geq 1 \end{cases} \tag{27}$$

5 Conclusion

Calculations made on contacts under ZEV condition subjected to a load ramp show the respective influence of the viscosity wedge and squeeze effects. In steady-state conditions, the viscosity wedge is able to sustain a long-lasting film thickness. For very low loads corresponding to the hydrodynamic regime, an increase in the load leads to a fast decrease of the film thickness, whereas for high loads corresponding to the elastohydrodynamic regime, an increase of the load leads to an increase in the minimum film thickness. The change between regimes is therefore marked by a minimum value of the minimum film thickness. On the other hand, in transient isothermal conditions, the squeeze effect is only able to slow down the decrease of the film thickness. The faster the loading process, the stronger this effect.

A reference configuration in transient thermal condition shows how the squeeze effect can delay the decrease of the film thickness up to the point where the elastohydrodynamic regime is reached and strong temperature differences appear. From there, the viscosity wedge leads to a long-term film thickness up to the steady state.

A characteristic transient–thermal ratio is introduced to study the relative influence of the squeeze and thermal effects depending on the loading time.

For slow loadings, the thermal time is negligible in front of the loading time, which means that the contact closely follows the steady-state reference. In this range, the faster the loading, the stronger the initial squeeze effects, which increases the minimum film thickness.

For fast loadings, the contact is subjected to squeeze effects and the film thicknesses stays thick well after the maximum load is reached. This leaves enough time for the thermal effects to appear. As such, the minimum film thickness stays close to the steady-state reference at final load, which can be estimated by a prediction formula inspired from [23].

Finally, under intermediate loadings, the initial separation provided by the squeeze effect is significant. The squeeze effect still fades out before the maximum load is reached. Meanwhile, thermal effects become really dominant after a given time. This leads to low values of the minimum film thickness over time. It is shown that this value can be estimated by an adaptation of the model from Wang et al. [19] considering only the squeeze effect.

Appendix: Semi-analytical Formula for the Prediction of the Minimum Film Thickness in Steady-State ZEV Contacts

As described in Eqs. 19 and 20, a semi-analytical model was employed to attempt a prediction of the minimum film thickness under steady-state ZEV condition. The given formula was established using the experimental and numerical data measured in [23]. The corresponding study focused on

Table 10 Material properties for the sapphire disk used in [23]

Parameter	Value
E_2 (Pa)	360×10^9
υ_2	0.34
ρ_2 (k g m^{-3})	4000
Cp_2 (J k g^{-1}K^{-1})	750
k_2 (W m^{-1} K^{-1})	40

Table 11 Input data for the experimental and numerical campaign initially used in [23]. For each configuration, experimental and numerical results were obtained, except for the two lower loads noted (*) for which only numerical results were obtained

u (m/s)	R_{eq} (m)	T_0 (K)	w_{ref} (Nm^{-1})
1.77;1.99;2.26;2.51;2.81; 3.16;3.54;3.97;4.46;5.00; 5.61;6.30;7.06;7.92;8.89; 9.98;11.19;12.56;14.09; 15.09;17.74	0.0128	293.15	$1.99 \times 10^{4(*)}$
			$3.16 \times 10^{4(*)}$
			4.14×10^4
			5.82×10^4
			9.24×10^4

the minimum film thickness in contacts between a sapphire disk and a steel barrel under ZEV condition. With 293.15K boundary temperature, the relative difference between the model and the experimental results stays below 16%. This study showed that in the present range of conditions, steel on steel contacts are similar to sapphire on steel ones and

their respective minimum film thicknesses are close enough. Complementary calculations were conducted at lower loads in order to expand the range of the study. For material data on the lubricant and steel, refer to Tables 1 and 2, respectively. The material data for sapphire are listed in Table 10. The remaining input conditions are listed in Table 11.

Using these values, a curve-fit was established using the method of least squares, as given in Eqs. 28 and 29. This model is confronted to the numerical and experimental results in Fig. 12. The coefficient of determination for the experimental dataset is 0.96; for the numerical dataset, it is 0.98.

$$\frac{h_m^{A*}(u, w)}{h^*} = w^{0.146} \times (1 - \exp(-u/u^*)) \tag{28}$$

$$\frac{u^*}{u_0} = 1 + \exp\left(-\frac{w}{w_0}\right) \tag{29}$$

where w is expressed in N m^{-1}, $h^* = 69.8$ nm, $u_0 = 2.74$ ms^{-1}, $w_0 = 14695$ Nm^{-1}.

The factor $\left(\frac{R_{eq}}{R^*}\right)^{-0.42}$ found in Eq. 19 was determined by the method of least squares, using the simulation results of Case A and the partial model given in Eqs. 28 and 29. Because the exponent -0.42 was determined with only two radii, and because these radius values are so close (0.01 m and 0.0128 m), extreme precaution should be taken when using the formula in Eq. 19 if one would apply it to very different radius values.

Fig. 12 Ratio of the minimum film thickness over the value of h^* as a function of the ratio of the velocity over u^*
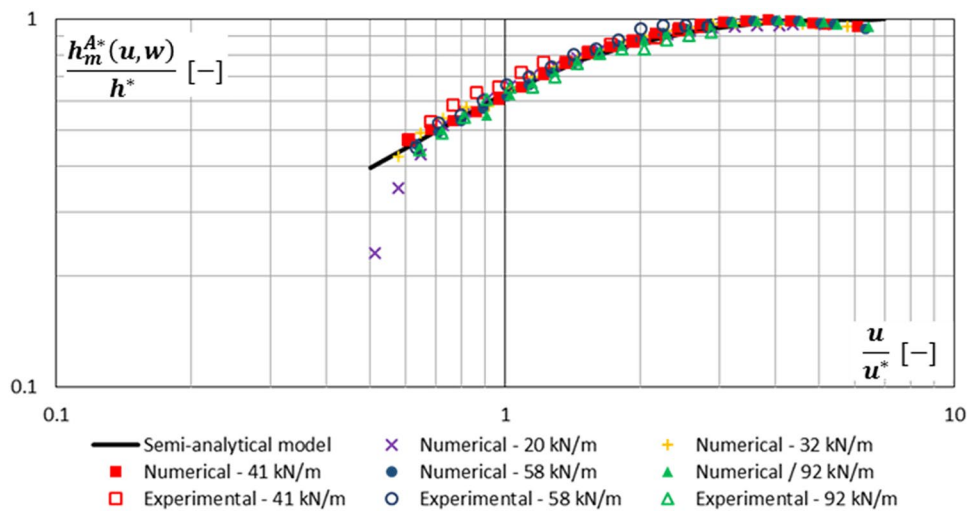
References

1. Ertel, A.M.: In Russian (hydrodynamic lubrication based on new principles). Nauk SSSR Prikadnaya Math. I Mekhanika **3**(2), 41–52 (1939)

2. Grubin, A.N., Vinogradova, I.E.: In Russian (Investigation of the contact of machine components). Cent. Sci. Res. Inst. Technol. Mech. Eng. **30**, 1–2 (1949)

3. Hamrock, B.J., Dowson, D.: Isothermal elastohydrodynamic lubrication of point contacts-I-theorectical formulation. J. Lubr. Tech. **98**(2), 223–228 (1976)

4. Hamrock, B.J., Dowson, D.: Isothermal elastohydrodynamic lubrication of point contacts-III-fully flooded results. J. Lubr. Tech. **99**(2), 264–275 (1977)

5. Hamrock, B.J., Dowson, D.: Isothermal elastohydrodynamic lubrication of point contacts-IV-starvation results. J. Lubr. Tech. **99**(1), 15–23 (1977)

6. Moes, H.: Optimum similarity analysis with applications to elastohydrodynamic lubrication. Wear **159**(1), 57–66 (1992)

7. Chittenden, R.J., Dowson, D., Dunn, J.F., Taylor, C.M.: A theoretical analysis of the isothermal elastohydrodynamic lubrication of concentrated contacts I: direction of lubricant entrainment coincident with the major axis of the hertzian contact ellipse. Proc. R. Soc. A **397**(1813), 245–269 (1985)

8. Evans, H.P.: The isothermal elastohydrodynamic lubrication of spheres. J. Tribol. **103**(4), 547 (1980)

9. Venner, C.H.: Multilevel solution of the EHL line and point contact problems. [Ph.D. Thesis] Enschede. University of Twente, (1991)

10. Bruyere, V., Fillot, N., Morales-Espejel, G.E., Vergne, P.: Computational fluid dynamics and full elasticity model for sliding line thermal elastohydro dynamic contacts. Tribol. Int. **46**(1), 3–13 (2012)

11. Raisin, J., Fillot, N., Dureisseix, D., Vergne, P., Lacour, V.: Characteristic times in transient thermal elastohydrodynamic line contacts". Tribol. Int. **82**, 472–483 (2015)

12. Cameron, A.: The viscosity wedge. ASLE Trans. **1**(2), 248–253 (1958)

13. Jones, W.R.J., Shogrin, B.A., Kingsbury, E.P.: Long term performance of a retainerless bearing cartridge with an oozing flow lubricator for spacecraft applications. *NASA TM-107492*. (1997)

14. Shogrin, B.A., Jones, W.R., Kingsbury, E.P.P., Jansen, M.J., Prahl, J.M.: Experimental study of load carrying capacity of point contacts at zero entrainment velocity. *NASA TM-208650*. (1998)

15. Shogrin, B.A., Jones, W.R., Kingsbury, E.P., Prahl, J.M.: Experimental determination of load carrying capacity of point contacts at zero entrainment velocity. *NASA TM-208848*. (1999)

16. Thompson, P.: The effect of sliding speed on film thickness and pressure supporting ability of a point contact under zero entrainment velocity conditions. *NASA TM-210566*, (2000)

17. Guo, F., Wong, P.L., Yang, P., Yagi, K.: Film formation in EHL point contacts under zero entraining velocity conditions. Tribol. Trans. **45**(4), 521–530 (2002)

18. Zhang, B., Wang, J.: Enhancement of thermal effect in zero entrainment velocity contact under low surface velocity. Proc. Inst. Mech. Eng. Part J **230**(12), 1554–1561 (2016)

19. Zhang, B., Wang, J., Omasta, M., Kaneta, M.: Variation of surface dimple in point contact thermal EHL under ZEV condition. Tribol. Int. **94**, 383–394 (2016)

20. Guo, F., Yang, P., Wong, P.L.: On the thermal elastohydrodynamic lubrication in opposite sliding circular contacts. Tribol. Int. **34**(7), 443–452 (2001)

21. Yagi, K., Kyogoku, K., Nakahara, T.: Relationship between temperature distribution in EHL film and dimple formation. J. Tribol. **127**(3), 658 (2005)

22. Zhang, B., Wang, J., Omasta, M., Kaneta, M.: Effect of fluid rheology on the thermal EHL under ZEV in line contact. Tribol. Int. **87**, 40–49 (2015)

23. Meziane, B., Vergne, P., Devaux, N., Lafarge, L., Morales-Espejel, G.E., Fillot, N.: Film thickness build-up in zero entrainment velocity wide point contacts. Tribol. Int. **141**, 105897 (2020)

24. Dowson, D., Jones, D.A.: Lubricant entrapment between approaching elastic solids. Nature **214**(5091), 947–948 (1967)

25. Safa, M.M., Gohar, R.: Squeeze films in elastohydrodynamic lubrication. Leeds–Lyon Symposium on Tribology. **10**, 227–233 (1985).

26. Larsson, R., Höglund, E.: Elastohydrodynamic lubrication at pure squeeze motion. Wear **179**(1–2), 39–43 (1994)

27. Dowson, D., Wang, D.: Impact elastohydrodynamics. Tribol. Ser. **30**, 565–582 (1995)

28. Wang, J., Venner, C.H., Lubrecht, A.A.: Central film thickness prediction for line contacts under pure impact. Tribol. Int. **66**, 203–207 (2013)

29. Venner, C.H., Wang, J., Lubrecht, A.A.: Central film thickness in EHL point contacts under pure impact revisited. Tribol. Int. **100**, 1–6 (2016)

30. Wong, P.L., Li, X.M., Guo, F.: Evidence of lubricant slip on steel surface in EHL contact. Tribol. Int. **61**, 116–119 (2013)

31. Li, X.M., Guo, F., Wong, P.L.: Shear rate and pressure effects on boundary slippage in highly stressed contacts. Tribol. Int. **59**, 147–153 (2013)

32. Wheeler, J.-D., Fillot, N., Vergne, P., Philippon, D., Morales Espejel, G.: On the crucial role of ellipticity on elastohydrodynamic film thickness and friction. Proc. Inst. Mech. Eng. Part J. **230**(12), 1503–1515 (2016)

33. Habchi, W.: A full-System Finite Element Approach to Elastohydrodynamic Lubrication Problems: Application to Ultra-low-viscosity Fluids. Lyon, Institut National des Sciences Appliquées de Lyon (2008)

34. Hertz, H.: Ueber die Berührung fester elastischer Körper. J. für die reine und Angew. Math. (Crelle's J.) **1882**(92), 156–171 (1882)

35. Murnaghan, F.D.: The compressibility of media under extreme pressures. Proc. Natl. Acad. Sci. **30**(9), 244–247 (1944)

36. Bair, S., Mary, C., Bouscharain, N., Vergne, P.: An improved Yasutomi correlation for viscosity at high pressure. Proc. Inst. Mech. Eng. Part J. **227**(9), 1056–1060 (2013)

37. Bair, S.: A rough shear-thinning correction for EHD film thickness. Tribol. Trans. **47**(3), 361–365 (2004)

38. Dowson, D.: A generalized Reynolds equation for fluid-film lubrication. Int. J. Mech. Sci. **4**(2), 159–170 (1962)

39. Wheeler, J.-D., Molimard, J., Devaux, N., Philippon, D., Fillot, N., Vergne, P., Morales-Espejel, G.E.: A generalized differential colorimetric interferometry method: extension to the film thickness measurement of any point contact geometry. Tribol. Trans. **61**(4), 648–660 (2018)

40. Doki-Thonon, T., Fillot, N., Vergne, P., Morales Espejel, G.E.: Numerical insight into heat transfer and power losses in spinning EHD non-Newtonian point contacts. Proc. Inst. Mech. Eng. Part J **226**(1), 23–35 (2012)

41. Ndiaye, S.-N., Martinie, L., Philippon, D., Devaux, N., Vergne, P.: A quantitative friction-based approach of the limiting shear stress pressure and temperature dependence. Tribol. Lett. **65**(4), 149 (2017)

42. Kaneta, M., Nishikawa, H., Mizui, M., Guo, F.: Impact Elastohydrodynamics in Point Contacts. Proc. Inst. Mech. Eng. Part J. **225**(1), 1–12 (2011)

43. Kaneta, M., Wang, J., Guo, F., Krupka, I., Hartl, M.: Effects of loading process and contact shape on point impact elastohydrodynamics. Tribol. Trans. **55**(6), 772–781 (2012)

44. Reynolds, O.: IV. On the theory of lubrication and its application to Mr. Beauchamp tower's experiments, including an experimental

determination of the viscosity of olive oil. Philos. Trans. R. Soc. Lond. **177**, 157–234 (1886)

45. Bair, S.: Correlations for the Temperature and Pressure and Composition Dependence of Low-Shear Viscosity. In *High Pressure Rheology for Quantitative Elastohydrodynamics*, Elsevier, 135–182 (2019)

46. Vichard, J.P.: Transient effects in the lubrication of hertzian contacts. J. Mech. Eng. Sci. **13**(3), 173–189 (1971)

Publisher's Note Springer Nature remains neutral with regard to jurisdictional claims in published maps and institutional affiliations.